The Astrophysical Journal, 926:176 (7pp), 2022 February 20 https://doi.org/10.3847/1538-4357/ac4810

X-Ray-induced Diffusion and Mixing in Layered Astrophysical Ices

Antonio Jiménez-Escobar[1], Angela Ciaravella[1], Cesare Cecchi-Pestellini[1], Guillermo M. Muñoz Caro[2], Chao-Hui Huang[3], Ni-En Sie[3], and Yu-Jung Chen[3]
[1] INAF—Osservatorio Astronomico di Palermo, P.za Parlamento 1, I-90134 Palermo, Italy; antonio.jimenez@inaf.it
[2] Centro de Astrobiología (INTA-CSIC), Ctra. de Ajalvir, km 4, E-28850 Torrejón de Ardoz, Madrid, Spain
[3] Department of Physics, National Central University, Jhongli City, Taoyuan County 32054, Taiwan, em2; asperchen@phy.ncu.edu.tw
Received 2021 September 23; revised 2021 December 19; accepted 2022 January 3; published 2022 February 23

Abstract

Ice in cold cosmic environments is expected to be organized in a bilayered structure of polar and apolar components. The initial water-rich layer is embedded in an icy CO envelope, which provides the feedstock for methanol formation through hydrogenation. These two components are thought to be physically segregated, unless an increase in temperature favors mobility and reactivity within the ice. We present new and robust evidence of X-ray-induced diffusion within interstellar ice analogues at very low temperatures, leading to an efficient mixing of the molecular content of the ice. The results of our study have two main implications. First, molecular mixing enhances chemical reactions from which complex organic species, including many of prebiotic interest, are formed. Second, diffusion drives the desorption of species that would otherwise remain buried near the surface of dust, thus enhancing their abundances in the gas, where they can be detected in the radio-wave domain. Such a scenario may have implications for the chemical history of ices in protoplanetary disks, in particular in the early stages of their life.

Unified Astronomy Thesaurus concepts: Laboratory astrophysics (2004); Protoplanetary disks (1300); Molecular physics (2058); Pre-biotic astrochemistry (2079)

1. Introduction

In cold interstellar regions, dust grains accrete atoms and molecules from the surrounding gas. Observational data constrain both the chemical compositions of these ices and their physical structure (e.g., Boogert et al. 2015). Water is the dominant component of the ice in dense interstellar regions (e.g., Ehrenfreund & Schutte 2000), and it is supposed to form by hydrogenation of simple oxygen-bearing precursors (see, e.g., van Dishoeck et al. 2013 and references therein). Such a water-rich ice layer condenses early in the evolution of a cloud, and includes the bulk of solid CH_4 and NH_3; they too likely formed through hydrogenation of carbon and nitrogen (e.g., Qasim et al. 2020). In this phase, methanol formation may proceed through OH-mediated reactions of methane (Qasim et al. 2018). However, the bulk of methanol formation is supposed to occur later on, in the collapse of a cloud to form stars, during the CO freeze-out stage. The formation of a CO ice layer provides the feedstock for the formation of icy methanol and other organics through recombination of free radicals formed via H-atom addition and abstraction reactions at different steps in the hydrogenation chain $CO \rightarrow H_2CO \rightarrow CH_3OH$ (Chuang et al. 2016).

Energetic processing of dust icy mantles induces the synthesis of complex molecules that may desorb to enrich the gas phase. Chemical reactions need mobility of the reactants either on the surface or within the ice. Bulk species desorption may take place if these species travel toward the surface and leave the ice. In both cases diffusion needs to occur (Garrod 2013). Thermal ice diffusion has been the subject of a few experimental studies (e.g., Cooke et al. 2018), while there is little experimental evidence of diffusion and mixing sustained by radiation inside astrophysical ice analogues. Such a possibility has been briefly mentioned in Pilling et al. (2019), in experiments involving soft X-ray irradiation of water-rich ices. Laboratory studies of (∼500 eV) electron irradiation (Gadallah et al. 2017) suggest that molecular hydrogen together with its isotopic substitutions may migrate within a water ice matrix, reaching the surface and eventually desorbing. Similar conclusions have been reached by Ciaravella et al. (2020) through experiments involving soft X-ray irradiation of composite ices, this time involving the diffusion of heavier species such as, e.g., CO and CO_2.

In this work, we present new and robust evidence of X-ray-induced diffusion within ices of mixed composition. We consider stratified, two-layer ices, in which an inner mixture of H_2O, CH_4, and NH_3 is covered by a mixed mantle of CO and CH_3OH. While this representation has a straightforward application to dense interstellar regions illuminated by an X-ray source (e.g., a massive star or X-ray binaries), it may have implication for the solid and gas chemical abundances of protoplanetary disks in the first few million years. During this epoch, the central star emits primarily X-rays (Ribas et al. 2005), which permeate the outer disk regions where ice-covered dust grains are present.

Infrared features of stratified ice analogs are in good agreement with CH_3OH observations toward prestellar cores and star-forming regions (Müller et al. 2021). The presence of stratified ices in protoplanetary disks is debated (e.g., Booth et al. 2021). Cometary ices resemble the composition of interstellar ice mantles, suggesting that such ice mantles could be preserved in some regions of disks, as a few theoretical and experimental studies seem to support (e.g., Bergner & Ciesla 2021). In the opposite case, if ices are formed from scratch on top of bare grains, the condensation would occur while dust particles experience temperature gradients during

their motion within the disk. Thus, a first layer of H_2O and other relatively refractory species could be formed. On top of this layer, volatile molecules like CO would accrete. Whatever the case may be, it is of interest to perform simulations reflecting both inherited and fully reset chemical initial conditions, because the James Webb Space Telescope will put stringent constraints on the layered or mixed nature of ices in different interstellar environments (see, e.g., the models presented in Ballering et al. 2021).

In the next section we present the experiments, and the facility we use to perform them. Sections 3 and 4 contain the results of laboratory simulations. They are discussed in the last section, where we also draw our conclusions, and we consider possible astrophysical implications.

2. Experiments

The ice experiments described in this paper have been performed with the Interstellar Energetic-Process System (IEPS) facility (Huang et al. 2020). IEPS is an ultrahigh vacuum chamber of base pressure 5×10^{-10} Torr (67 nPa), where the sample is made by deposition of a gas mixture onto an infrared transparent window mounted on a cold finger at 11 K. The evolution of the ice is monitored by in situ transmittance Fourier transform infrared spectroscopy, while volatile species are detected through a quadrupole mass spectrometer (QMS).

The samples are double-layer ices accreted on a CaF_2 substrate at 11 K. A first layer of H_2O:$^{13}CH_4$:$^{15}NH_3$ (2:1:1) mixture is covered by a CO:CH_3OH (3:1) mixture. H_2O purchased from Merck, LC MS grade, $^{13}CH_4$ (99% atomic ^{13}C) from Specialty Gases of America, $^{15}NH_3$ (98% atomic ^{15}N) from Cambridge Isotope Laboratories Inc., CH_3OH of 99.9% purity from Merck, and CO of 99.9% purity from Cingfong Gas Industrial.

We irradiate the ice samples with a soft X-ray spectrum from the beamline BL08B at the National Synchrotron Radiation Research Center (NSRRC, Taiwan). The spectrum covers photon energies from 250 to 1250 eV, with a flux of 9.3×10^{15} photon s^{-1} cm^{-2}. We ran three experiments with the same bottom layer of 2500 ML and three different thicknesses of the top layer, i.e., 465 ML (experiment T1), 954 ML (experiment T2), and 1470 ML (experiment T3). 1 ML (monolayer) is defined as the thickness of one molecule corresponding to a column density of 1×10^{15} molecules cm^{-2}. The irradiation is performed in steps for a total time of 120 minutes in T1, 180 minutes in T2, and 270 minutes in T3.

The thickness T of the ice is obtained from the infrared spectra as

$$T = \frac{1}{10^{15}} \sum_{i=1}^{l} N_i \text{ ML}, \quad T = \frac{1}{N_A} \sum_{i=1}^{l} \frac{N_i \times M_i}{n_i} \times 10^7 \text{ nm} \qquad (1)$$

where $N_i = \frac{1}{A} \int_{\Delta\nu} \tau_\nu d\nu$ is the column density of the ith species, τ_ν the optical depth, and A the infrared band strength. i runs over all the l species present in the mixture of each layer. N_A is the Avogadro number, and M_i and n_i are the atomic mass and the density of the ith species, respectively. The densities adopted for CO, CH_3OH, and CO_2 are $n_{CO} = 0.80$ g cm^{-3}, $n_{CH_3OH} = 1.01$ g cm^{-3}, and $n_{CO_2} = 1.11$ g cm^{-3} (Bouilloud et al. 2015). We also adopt the band strengths $A_{CO} = 1.1 \times 10^{-18}$ cm molecule^{-1} at 2136 cm^{-1} (Jiang et al. 1975), $A_{CH_3OH} = 1.8 \times 10^{-17}$ cm molecule^{-1} at 1026 cm^{-1} (D'Hendecourt et al. 1986), $A_{CO_2} = 7.6 \times 10^{-17}$ cm molecule^{-1} at 2343 cm^{-1} (Jiang et al. 1975), and $A_{H_2O} = 1.5 \times 10^{-16}$ cm molecule^{-1} at 3033 cm^{-1} (Bouilloud et al. 2015). For $^{13}CH_4$ and $^{15}NH_3$ we use the values of the band strengths of $^{12}CH_4$ and $^{14}NH_3$ since no specific values have been found in the literature. These values are $A_{CH_4} = 8 \times 10^{-18}$ cm molecule^{-1} (Bouilloud et al. 2015) at 1303 cm^{-1}, and $A_{NH_3} = 1.63 \times 10^{-17}$ cm molecule^{-1} (Bouilloud et al. 2015) at 1070 cm^{-1}. The band of H_2O at ~3033 cm^{-1} is blended with those of $^{13}CH_4$ at ~3010 cm^{-1} ($A_{CH_4} = 1.1 \times 10^{-17}$ cm molecule^{-1}, Bouilloud et al. 2015) and $^{15}NH_3$ at ~3376 cm^{-1} ($A_{NH_3} = 2.3 \times 10^{-17}$ cm molecule^{-1}, Bouilloud et al. 2015). We obtain the integrated absorbance of the $^{13}CH_4$ and $^{15}NH_3$ by scaling the values for the band at 1303 cm^{-1} and 1070 cm^{-1} by the ratio of the band strengths. We compute the integrated absorbance of H_2O by subtracting the contribution of the $^{13}CH_4$ and $^{15}NH_3$.

3. Results

Infrared spectra of the ice before and at the end of the irradiation are shown in Figure 1 (left panels). X-ray photons have different penetration length through the ice. Photons of higher energy penetrate deeper into the ice than those of lower energy. The attenuation of the spectrum as a function of the photon energy E and the penetration length l inside the top layer is given by

$$I(E, l) = I(E, l_0) \times e^{-\tau_E(l)} \qquad (2)$$

where $I(E, l_0)$ is the spectrum that hits the sample and $\tau_E(l)$ the optical depth. We estimate the attenuation of the X-ray spectrum using the tool available at http://henke.lbl.gov based on scattering, transmission, and photoabsorption coefficients by Henke et al. (1993). The penetration length at which 95% of the photons of a given energy are absorbed inside ice of the same initial composition as the top layer is about 1630, 2760, 7749, and 16,710 nm for photons of energy 300, 600, 900, and 1200 eV, respectively. Such values are significantly larger than the top layer thicknesses we use in our experiments, e.g., at 600 eV the X-ray flux is reduced by 25% in T1 and 50% in T3. Thus, a significant fraction of the photons that hit the sample reach the deepest regions of the ice, inducing the formation of new species in the bottom layer that appear in the infrared spectra since the first irradiation step.

During the irradiation, we detect desorption of both parent molecules and their products. The species from the top layers desorb first (Figure 1, right panels): CO ($m/z = 28$) and the main product of the top layer, CO_2 ($m/z = 44$), show desorption peaks starting from the beginning of the irradiation (Chen et al. 2013; Ciaravella et al. 2020). Methanol is very quickly converted into new species, and it has a negligible photodesorption as shown in the first irradiation steps of $m/z = 31$, this being the main methanol fragment measured by QMS. The photodesorption of the species in the top layer decreases with the irradiation time as typically observed in X-ray experiments (Jiménez-Escobar et al. 2018; Ciaravella et al. 2019). The sudden increase of $m/z = 29$ and 45 from the negligible values compatible with the natural ^{13}C isotopic abundance of CO and CO_2 in the top layer provides evidence of ^{13}CO and $^{13}CO_2$ desorbing from the bottom layer. Since

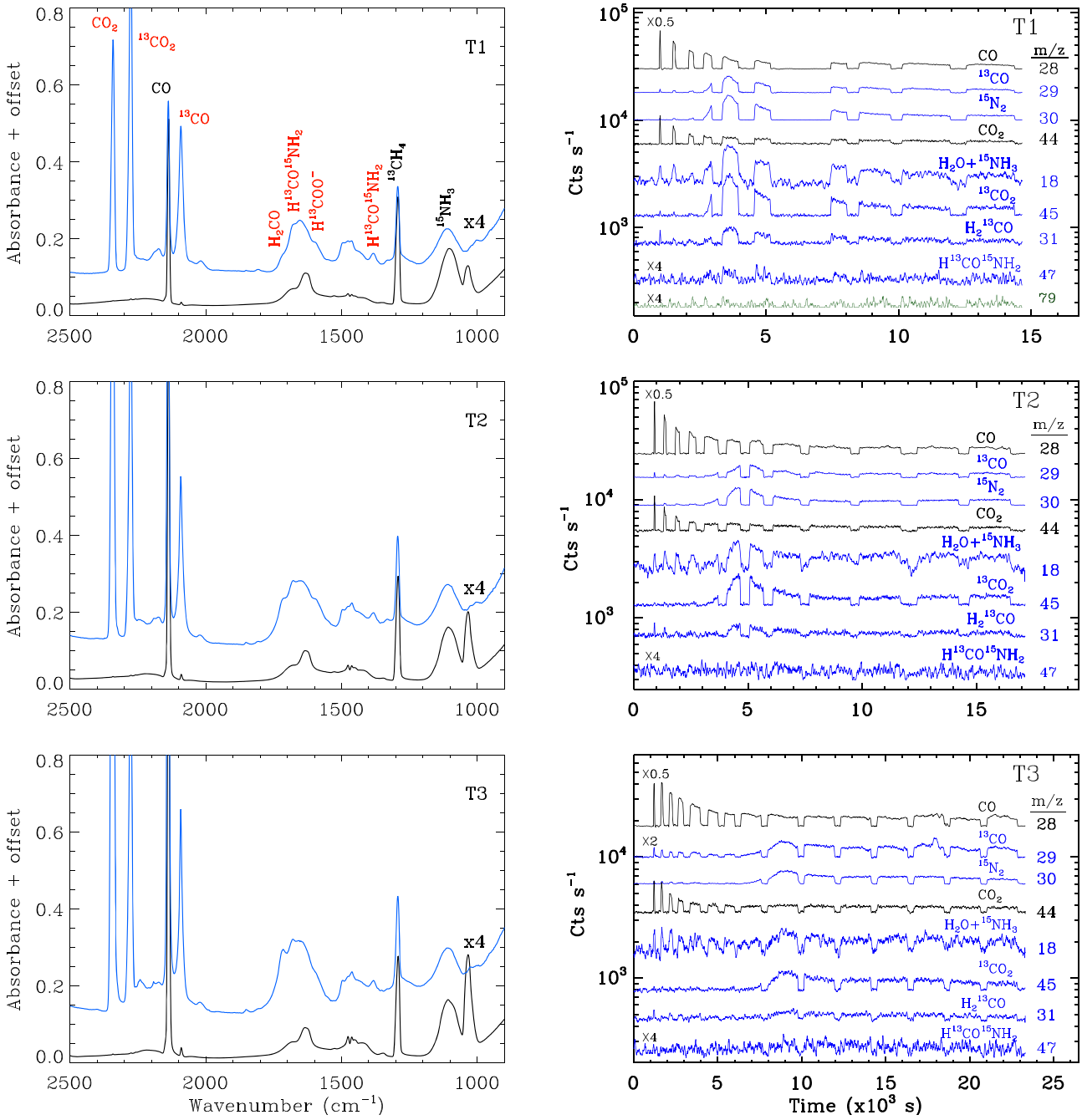

Figure 1. Left panels: infrared spectra of the ices for the experiments T1 (top), T2 (middle), and T3 (bottom), before (black lines) and after irradiation (blue lines, multiplied by 4). Right panels: main photodesorbing fragments detected by the QMS during soft X-ray irradiation for the three experiments. CO ($m/z = 28$) and CO_2 ($m/z = 44$) (black curves) come from the top layer. ^{13}CO ($m/z = 29$), $^{13}CO_2$ ($m/z = 45$), $^{15}N_2$ ($m/z = 30$), $H_2{}^{13}CO$ ($m/z = 31$), H_2O and $^{15}NH_3$ ($m/z = 18$), and $H^{13}CO^{15}NH_2$ and possibly $H^{13}COOH$ ($m/z = 47$) come from the bottom layer. For comparison with $m/z = 47$, the top panel shows the spectrum of $m/z = 79$ (green line), a value at which no species are expected.

$m/z = 31$ has a negligible contribution from CH_3OH (Cruz-Diaz et al. 2016; Ciaravella et al. 2020), $H_2{}^{13}CO$ from the bottom layer dominates the mass spectrum. In the first few irradiation steps $m/z = 30$ is due to H_2CO from the top layer, but the sharp increase detected in all the experiments suggests a significant contribution from the bottom layer species $^{15}N_2$. $m/z = 47$ is very noisy, but in the experiment with the thinnest top layer, T1, it shows a similar behavior to other species coming from the bottom layer. Also shown for comparison is $m/z = 79$, a blank value at which no species are expected. $m/z = 47$ could be associated with either formamide $H^{13}CO^{15}NH_2$ or formic acid $H^{13}COOH$. Along with the products of the irradiation from the bottom layer we detected the desorption of the three parent molecules. In the right panels we report the spectra for $m/z = 18$ corresponding to H_2O and $^{15}NH_3$. The increases in the ion counts of $m/z = 18$, 29, 30, 31, 45, and 47 mark the starting time of the photodesorption of the bottom layer species.

Molecular diffusion within the ice will be estimated using the species with the highest QMS signal-to-noise ratio: ^{13}CO, $^{13}CO_2$, $^{15}N_2$, and $H_2{}^{13}CO$. In the top panel of Figure 2 are plotted the top layer thicknesses as a function of the integrated

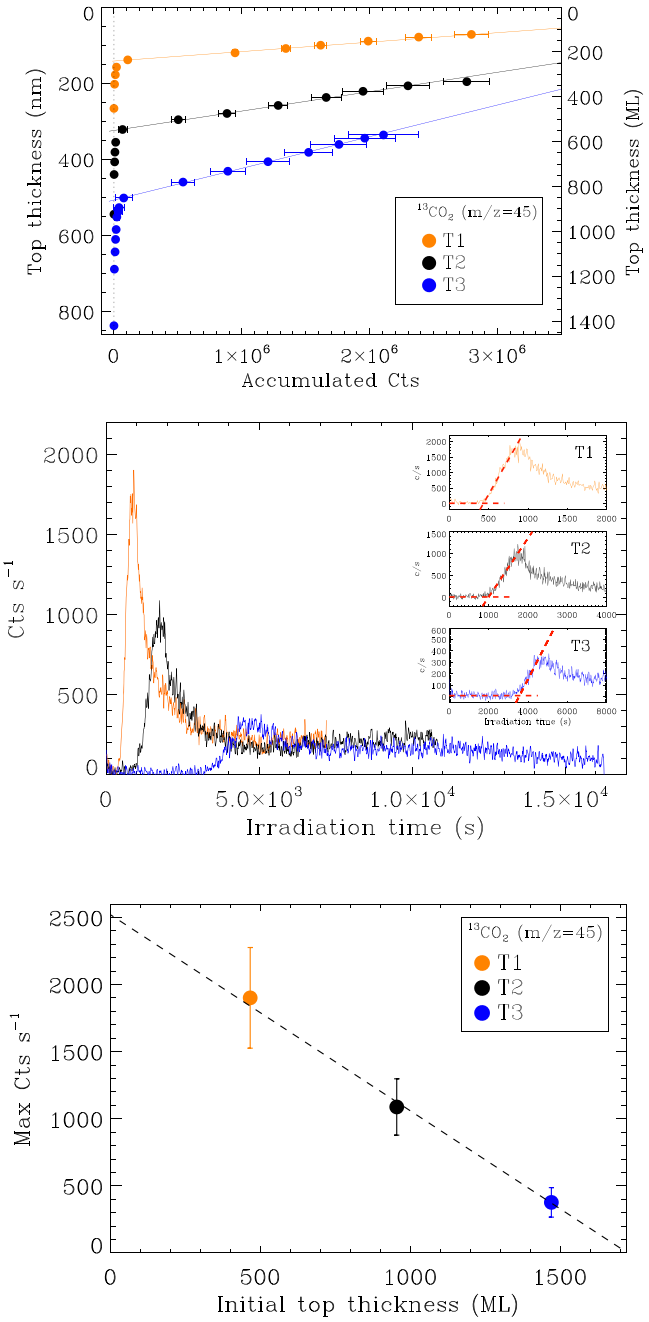

Figure 2. Top panel: top layer thickness in nm (left axis) and ML (right axis) as a function of the accumulated ion current of $^{13}CO_2$ ($m/z = 45$). The three curves are for the experiments with top layer thickness of 465 ML (orange), 954 ML (black), and 1470 ML (blue). Middle panel: ion count rate for $^{13}CO_2$ ($m/z = 45$) as a function of the irradiation time. In these curves the idle time between two consecutive irradiation steps (see right panels in Figure 1) has been removed. The insets show the region in which the contributions of the bottom layer begin to appear. Bottom panel: peak values of $^{13}CO_2$ ($m/z = 45$) for the three experiments as a function of the top layer thickness at the time of their detection. The error bars are the statistical error in the QMS spectra.

counts of the bottom layer species $^{13}CO_2$ ($m/z = 45$) for the three experiments. The top layer thickness at each irradiation step is computed taking into account only the parent molecules CO and CH_3OH, and the main product CO_2; see Equation (1). Aside from CO_2 the other products of the irradiation are not used because they are highly blended (Figure 1, left panels). Thus, the top layer thicknesses are lower limits. From Figure 2 , the contributions to $m/z = 45$ from the bottom layer start when the top layer thicknesses are 236, 546, and 852 ML (42, 324, and 507 nm) for experiments T1, T2, and T3, respectively. The desorbing species travel through the top layer at least 142, 324, and 507 nm before reaching the surface of the ice. The middle panel of Figure 2 shows the mass spectra for $^{13}CO_2$ in which all the idle times between two consecutive irradiation steps shown in Figure 1 (right panels) have been removed. At long irradiation times the curves tend to similar values ($\sim$200 counts s^{-1}). This figure clearly highlights the dependence of the desorption of the bottom layer species on the top layer thickness: the desorption is much faster for the thinnest top layer (orange curve in Figure 2, middle panel). The starting time of the desorption (or diffusion time) has been computed by determining the intersection between the two red straight lines in the inlet panels. The horizontal line represents the negligible desorption of $m/z = 45$ from the top layer, while the ascending part is the $^{13}CO_2$ desorbing from the bottom layer. Thus, the starting times are 434, 996, and 3541 s for the experiments T1, T2, and T3, respectively.

The bottom panel in Figure 2 plots the maximum intensities of $m/z = 45$ in the middle panel as a function of the top layer thickness for experiments T1, T2, and T3, and the linear fit. The peak intensity decreases linearly as the top layer thickness increases. From the behavior observed in figure the desorption peak of the bottom species should disappear for a top thickness $\sim$1700 ML ($\sim$1000 nm), leaving a shallow increase followed by a residual desorption, like that detected at $\sim$6500 s (Figure 2, middle panel).

4. Diffusion

The desorption of the bottom layer species during irradiation suggests that diffusion induced by X-rays occurs inside the ice. The time at which the species desorb is a function of the top layer thickness (middle panel in Figure 2). We estimate the diffusion coefficient, D, of the four most abundant molecules as follows (Ghesquière et al. 2015):

$$\langle L^2 \rangle = q \times t \times D \quad (3)$$

where L is the diffusion length, t is the time required to travel the distance L, and q is a constant whose value is 2, 4, or 6 for one-, two-, or three-dimensional diffusion. We use $q = 6$. For the diffusion length we use the average of the upper and lower limits of the top layer thickness. The upper limit is the initial (sample) thickness of the top layer. The values of the lower limit are the thicknesses at the time we detect the desorption of the bottom layer species, computed as described in the previous section. The lower and upper limits of the thickness determine the error bars on the diffusion coefficient. Our estimate of the diffusion coefficients may be affected by uncertainties in the assumed values of relevant quantities, such as, e.g., variations in the ice structure and composition during the irradiation. This, in turn, affects the ice density and the molecular band strengths. According to literature data, variations in band strength are well within the 15%–20% uncertainties usually associated with them. Moreover, a more compact and denser ice will modify its thickness, and therefore affect diffusion coefficients. Using a density of the top layer 1.5 times larger than the values used in our calculation, we obtain a systematic decrease in the diffusion coefficients by about a factor of 4.

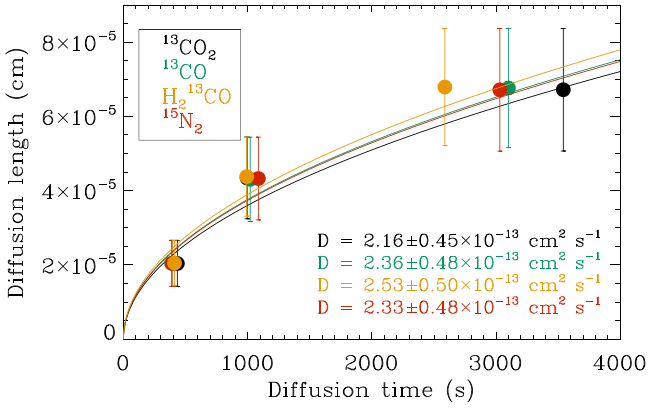

Figure 3. Diffusion coefficients obtained for $^{13}CO_2$, ^{13}CO, $^{15}N_2$, and $H_2^{13}CO$ in the three experiments. The error bars on the diffusion coefficients are related to the uncertainties in the estimate of the top layer thickness.

The new molecular species produced in the bottom layer during X-ray irradiation are detected in the infrared spectra since the first irradiation step. Therefore, we can assume that the time needed for a given species to diffuse through the top layer is the time at which this species is detected in the gas phase by the QMS (see Figure 2). Under this assumption we obtain the diffusion coefficient D by plotting the diffusion length as a function of the diffusion time and fitting the data by using Equation (3). The diffusion coefficients for $^{13}CO_2$, ^{13}CO, $^{15}N_2$, and $H_2^{13}CO$ are presented in Figure 3.

Within the uncertainties the diffusion induced by the soft X-ray photons used in our experiments is independent of the molecular species, $D \simeq 2.3 \times 10^{-13}$ cm^2 s^{-1}. The experimental data in Figure 1 show that the thicker the ice, the longer the time needed for a molecule in the bottom layer to reach the surface and desorb, and that within the same experiment the desorption is the same for all the bottom layer species.

5. Discussion and Astrophysical Implications

The soft X-ray irradiation of a double-layer ice induces photodesorption of parent molecules and new products from the bottom layer. Such a process is not instantaneous, with a delay due to the time needed for a bottom layer species to diffuse through the top layer and eventually reach the gas phase. The desorption/diffusion time lag increases with the thickness of the top layer and it is the same for all molecular species within the experimental error. A similar behavior is recorded in the desorption times of HD and D_2 during electron irradiation experiments on H_2O–D_2O layered ices around 100 K performed by Gadallah et al. (2017); these times appear to increase when the chemical source region is covered by progressively thicker caps of water ice. Since our experiments have been performed at temperatures $\lesssim$20 K, diffusion is largely nonthermal.

During the journey through the ice, some of the bottom layer species are likely to remain trapped inside the top layer (just as top layer species remain trapped within the bottom layer), where they can react with locally abundant species, giving rise to species of isotopic mixed compositions. In Figure 4 the infrared spectra of the experiments T1, T2, and T3, in the range 2140–2300 cm^{-1}, show some evidence of such chemical mixing. The bands associated with isocyanic acid and the OCN^- ion contain ^{15}N from the bottom layer and ^{12}C from the top layer. The spectra show that the abundances of the species

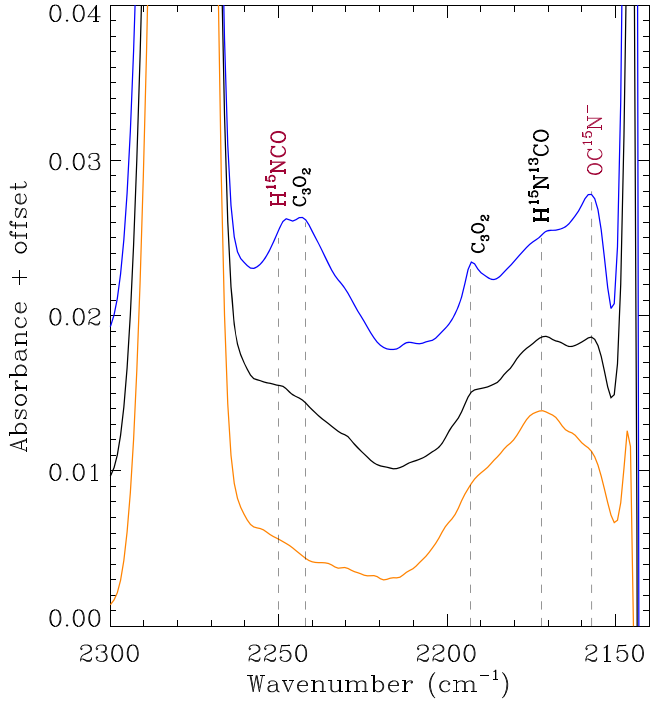

Figure 4. Infrared spectra in the range 2140–2350 cm^{-1} for experiments T1 (orange curve), T2 (black curve), and T3 (blue curve) in which the products of the irradiation are marked. Red labels show species made by components from both layers.

of mixed isotopic composition increase with the thickness of the top ice layer, proving that mixing does not occur only at the interface of the two layers.

The major results of this work are as follows (see Figure 5): (1) new species produced in the bottom layer diffuse into the top layer (as top layer species diffuse within the bottom layer) and eventually reach the gas phase; (2) diffusion times increase with the thickness of the top layer, and such times show negligible or no variations for different species; (3) diffusion inside the ice leads to the formation of species with mixed isotopic composition, further supporting the occurrence of molecular migration induced by X-ray processing; (4) the mixing of species originally residing in segregated chemical regions may partly reduce the stratification of the ice.

While nonthermal processing is a key mechanism for increasing chemical complexity in astrophysical ices, our results seem to suggest that high-energy irradiation may additionally promote migration within the ice at very low temperatures, increasing the mutual contamination of chemical regions that might originally be separate (as in the bilayered ice scenario). Such a process will necessarily impact on the gas-phase chemistry of evolving objects, as diffusion may drive the desorption of species that would otherwise remain buried near the surface of dust.

Dense molecular regions may be exposed to X-rays in a wide variety of astrophysical environments. The regions in which X-rays are the major ionization channel are called Röntgen spheres (Lorenzani & Palla 2001; Locci et al. 2018), and their evolution is dominated by the deposition of X-ray energy. In such conditions, the ice accumulated over dust grains may experience diffusion and mixing. First, without radiation-induced diffusion, at low temperatures photodesorbing species would be limited to the outskirts of the ice boundary. Second, without mixing, the thermal desorption temperatures of more

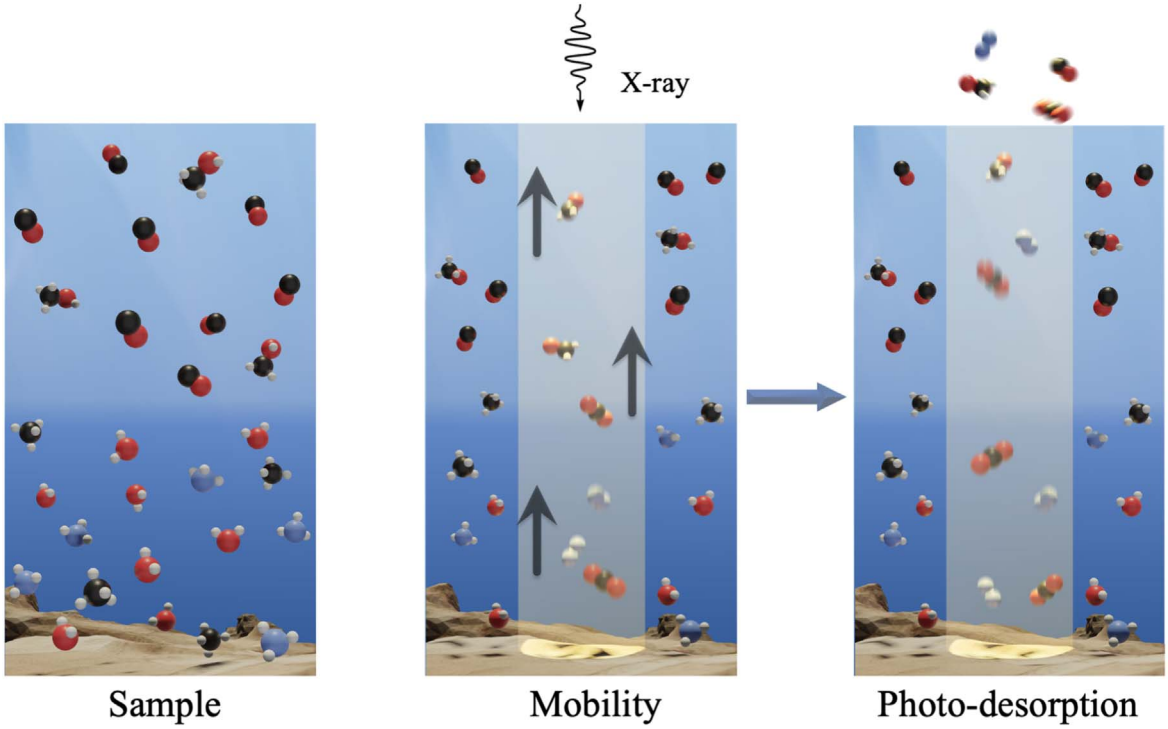

Figure 5. A bilayered ice accreted onto a CaF_2 window (sample) is irradiated by soft X-rays (yellow vertical cylinder). During the irradiation, species produced in the bottom layer diffuse within the top layer (mobility), allowing blending and chemical reactions among species of the two layers (mixing), and possibly release into the gas phase (desorption).

volatile species like CO and NH_3 would differ because mixing would dilute their segregation in the ice, so that they can form stronger bonds with H_2O and CH_3OH, and thus desorb at higher temperatures. Moreover, the chemistry induced by X-rays and later on by thermal annealing would be richer due to molecular mixing, as a larger number of different species are allowed to interact closely in the ice.

With the advent of the James Webb Space Telescope, it is of interest to predict the evolutionary history of ices in protoplanetary disks. One central question is that of the inheritance of the volatile component from the prestellar phase (e.g., Pontoppidan et al. 2014). Assuming that parts of the ices survive resetting in the coldest, less active regions of a disk (e.g., Booth et al. 2021), their interaction with the residual stellar X-ray flux at those locations may alter the previous chemical stratification. The results obtained in our experiment can be extrapolated to the disk midplane regions where the gas temperature is below 30 K. According to the model of Walsh et al. (2012) the expected quiescent X-ray emission from a young solar-type star is $\lesssim 10^{-4}$ erg cm^{-2} s^{-1}. We use the experiment T1 with the thinnest top layer of about 0.1 μm, a reasonable thickness for an ice mantle in the these regions of a disk, in which the diffusion time is 434 s (see Section 3). We estimate the diffusion time within the ice, t_D, by scaling the X-ray flux expected in the disk to that used in our experiment, to obtain $t_D \gtrsim 2$ Myr. This diffusion time could be shorter considering that young solar-type stars have a very frequent and often long-lasting (hours to days) flaring activity. Flares may increase the X-ray luminosity of the star by a few orders of magnitude, and may also increase its hardness (Favata et al. 2005).

We acknowledge the NSRRC general staff for running the synchrotron radiation facility. We also thank Dr. T.-W. Pi, the spokesperson of BL08B in NSRRC. The Spanish Ministry of Science, Innovation and Universities supported this research under grant number AYA2017-85322-R (AEI/FEDER, UE), and MDM-2017-0737 Unidad de Excelencia "María de Maeztu"–Centro de Astrobiología (INTA-CSIC), and the MOST grant MOST 110-2628-008-004-MY4 from Taiwan. We are grateful for the financial contribution from the agreement ASI-INAF n.2018-16-HH.0, Project "SPACE Tweezers" and ASI-INAF n.2021-5-HH.0. We finally thank Dr. T.-W. Liao (ORCID: 0000-0002-2019-6026) for drawing Figure 5.

ORCID iDs

Antonio Jiménez-Escobar https://orcid.org/0000-0003-3360-9333
Angela Ciaravella https://orcid.org/0000-0002-3127-8078
Cesare Cecchi-Pestellini https://orcid.org/0000-0001-7480-0324
Guillermo M. Muñoz Caro https://orcid.org/0000-0001-7003-7368
Chao-Hui Huang https://orcid.org/0000-0003-2741-2833
Ni-En Sie https://orcid.org/0000-0001-7755-7884
Yu-Jung Chen https://orcid.org/0000-0003-4497-3747

References

Ballering, N. P., Cleeves, L. I., & Anderson, D. E. 2021, ApJ, 920, 115
Bergner, J. B., & Ciesla, F. 2021, ApJ, 919, 45
Boogert, A. C. A., Gerakines, P. A., & Whittet, D. C. B. 2015, ARA&A, 53, 541

Booth, A. S., Walsh, C., Terwisscha van Scheltinga, J., et al. 2021, NatAs, 5, 684
Bouilloud, M., Fray, N., Bénilan, Y., et al. 2015, MNRAS, 451, 2145
Chen, Y. J., Ciaravella, A., Muñoz Caro, G. M., et al. 2013, ApJ, 778, 162
Chuang, K. J., Fedoseev, G., Ioppolo, S., van Dishoeck, E. F., & Linnartz, H. 2016, MNRAS, 455, 1702
Ciaravella, A., Jiménez-Escobar, A., Cecchi-Pestellini, C., et al. 2019, ApJ, 879, 21
Ciaravella, A., Muñoz Caro, G. M., Jiménez-Escobar, A., et al. 2020, PNAS, 117, 16149
Cooke, I. R., Öberg, K. I., Fayolle, E. C., Peeler, Z., & Bergner, J. B. 2018, ApJ, 852, 75
Cruz-Diaz, G. A., Martín-Doménech, R., Muñoz Caro, G. M., & Chen, Y. J. 2016, A&A, 592, A68
D'Hendecourt, L. B., Allamandola, L. J., Grim, R. J. A., & Greenberg, J. M. 1986, A&A, 158, 119
Ehrenfreund, P., & Schutte, W. A. 2000, AdSpR, 25, 2177
Favata, F., Flaccomio, E., Reale, F., et al. 2005, ApJS, 160, 469
Gadallah, K. A. K., Marchione, D., Koehler, S. P. K., & McCoustra, M. R. S. 2017, PCCP, 19, 3349
Garrod, R. T. 2013, ApJ, 778, 158
Ghesquière, P., Mineva, T., Talbi, D., et al. 2015, PCCP, 17, 11455
Henke, B. L., Gullikson, E. M., & Davis, J. C. 1993, ADNDT, 54, 181
Huang, C. H., Ciaravella, A., Cecchi-Pestellini, C., et al. 2020, ApJ, 889, 57
Jiang, G. J., Person, W. B., & Brown, K. G. 1975, JChPh, 62, 1201
Jiménez-Escobar, A., Ciaravella, A., Cecchi-Pestellini, C., et al. 2018, ApJ, 868, 73
Locci, D., Cecchi-Pestellini, C., Micela, G., Ciaravella, A., & Aresu, G. 2018, MNRAS, 473, 447
Lorenzani, A., & Palla, F. 2001, in ASP Conf. Ser. 243, From Darkness to Light: Origin and Evolution of Young Stellar Clusters, ed. T. Montmerle & P. André (San Francisco, CA: ASP), 745
Müller, B., Giuliano, B. M., Goto, M., & Caselli, P. 2021, A&A, 652, A126
Pilling, S., Rocha, W. R. M., Freitas, F. M., & da Silva, P. A. 2019, RSCAd, 9, 28823
Pontoppidan, K. M., Salyk, C., Bergin, E. A., et al. 2014, in Protostars and Planets VI, ed. H. Beuther et al. (Tuscon, AZ: Univ. Arizona Press), 363
Qasim, D., Chuang, K. J., Fedoseev, G., et al. 2018, A&A, 612, A83
Qasim, D., Fedoseev, G., Chuang, K. J., et al. 2020, NatAs, 4, 781
Ribas, I., Guinan, E. F., Güdel, M., & Audard, M. 2005, ApJ, 622, 680
van Dishoeck, E. F., Herbst, E., & Neufeld, D. A. 2013, ChRv, 113, 9043
Walsh, C., Nomura, H., Millar, T. J., & Aikawa, Y. 2012, ApJ, 747, 114